J Mater Sci (2016) 51:7843–7860

Phase evolution and crystallography of precipitates during decomposition of new "tungsten-free" Co(Ni)–Mo–Al–Nb γ–γ′ superalloys at elevated temperatures

S. K. Makineni[1,*], B. Nithin[1], D. Palanisamy[1], and K. Chattopadhyay[1]

[1] *Department of Materials Engineering, Indian Institute of Science, Bangalore 560 012, India*

Received: 6 February 2016
Accepted: 29 April 2016
Published online: 23 May 2016

ABSTRACT

This article reports the microstructural stability and consequent phase decomposition including the appearance of topologically close-packed (TCP) phases at high temperature of recently discovered tungsten-free γ–γ′ alloys of base composition Co–10Al–5Mo–2Nb with or without the addition of Ni and Ti. On prolonged aging at 800 °C of the Co–10Al–5Mo–2Nb alloy, needle-shaped DO_{19}-ordered precipitates with stoichiometry of Co_3(Mo, Nb) start appearing in the microstructure. In addition, growth of cellular domains from the grain boundaries featuring a three-phase composite lamellar structure could be observed. These phases are fcc γ-Co with composition different from the original matrix, CoAl with B2 ordering and Co_3(Mo, Nb) with DO_{19} ordering. All the phases exhibit well-defined crystallographic orientation relationships. The decomposition of the alloys depends on the solvus temperature of the γ′ phase. The Ni-containing alloy exhibits no phase decomposition until 100 h of aging at 800 °C without any significant effect on γ′ volume fraction (76 %). However, at 950 °C, the alloy decomposes leading to the appearance of four different phases including TCP phases: a Cr_3Si-type cubic phase, a hexagonal Laves phase, rhombohedral μ phase, and solid solution of Co phase. The γ–γ′ microstructure in the Co–10Al–5Mo–2Nb and Co–30Ni–10Al–5Mo–2Ta alloys is not stable at 800 and 950 °C, respectively, on long-term aging. This shows that the measured solvus temperatures (i.e., 866 and 990 °C) are metastable solvus temperatures. We also report that the Ti-containing alloy exhibits superior stability with no evidence of either TCP phase formation or any other decomposition of γ′ precipitates, even after aging at 950 °C for 100 h.

Address correspondence to E-mail: surendra.makineni@gmail.com

DOI 10.1007/s10853-016-0026-1

Introduction

Co-based superalloys featuring a γ–γ′ microstructure are receiving increasing attention as a possible alternative to Ni-based superalloys due to their comparable mechanical properties and improved high-temperature oxidation resistance [1–5]. Among these, alloys of Co–Al–W have been studied the most over the years through various methods such as alloying, processing, and evaluation of mechanical properties [6–8]. These alloys show uniform distribution of $L1_2$-ordered γ′ precipitates with cuboidal morphology and Co_3(Al, W) stoichiometry in a fcc γ-Co matrix [9, 10]. The morphologies and volume fractions of phases observed in the microstructures of these alloys are highly sensitive to alloying with elements like Ni, Ti, Mo, B, Cr, and Ta [11–16]. The thermodynamics and phase stability of the ordered γ′ structure have been studied using density functional theory (DFT) calculations by various groups [17–20]. These studies indicate that W is crucial for stabilizing the $L1_2$ structure of the γ′ phase giving rise to Co_3(Al, W) stoichiometry. The high-temperature strength improves significantly when Ta is added to Co–Al–W alloys. However, the presence of W and Ta in these alloys leads to higher densities (9.3–10.5 gm cm^{-3}) compared to Ni-based superalloys that have a similar γ–γ′ microstructure. Some reports state that Mo can replace up to 2 at.% W [21–23]. Further addition leads to the precipitation of needle-type Co_3Mo precipitates with DO_{19} structure that coexist with the $L1_2$-ordered γ′ Co_3(Al, W) precipitates in a fcc γ-Co matrix [24, 25]. The presence of these needle-type precipitates reduces the ductility and the alloy fractures in a brittle manner.

Recently, Co-based alloys with γ–γ′ microstructure that do not contain W were reported [26–28]. These are based on the composition Co–10Al–5Mo with small amounts of Nb or Ta and are further modified and developed by addition of Ni and Ti. The densities of Nb-containing alloys are in the range of 8.25–8.35 gm cm^{-3} which are much lower than in Co–Al–W-based as well as other Co-based alloys [29]. The reduction in density leads to higher specific 0.2 % yield strength compared to values observed in W containing Co–Al–W alloys. The solvus temperatures for the Co–10Al–5Mo–2Nb and the Co–30Ni–10Al–5Mo–2Nb alloys were found to be 866 °C and 990 °C, respectively [26, 27]. These alloys are a potential replacement for Co–Ni–Cr–W-based solid solution-strengthened alloys (such as Haynes 188) developed for application in the temperature range of 650–700 °C. Haynes 188 has good hot workability and excellent resistance to oxidizing environments combined with molten salt corrosion and sulfidation resistance due to their high content of Cr (∼20 wt%). But it exhibits low yield strength values (∼465 MPa) and high density (∼9.0 g cm^{-3}). Alloying additions such as Cr (for hot corrosion and oxidation), Ti with varying Al content can be used as a strategy to tune the volume fraction of γ′ in Co–Ni–Al–Mo–Nb-based alloys that will provide an option to control both hot workability and ductility. For high-temperature applications (>1000 °C), the solvus has to be increased beyond 1050 °C for these alloys. It is shown recently that replacing Nb with Ta and addition of Ti can lead to a solvus temperature >1050 °C [28]. This can be tuned further by other alloying additions such as Cr, Re, and Ru. Thus, there is a scope for further development of these alloys in future.

In this investigation, the microstructural changes that occur after prolonged aging at 800 °C are reported and discussed for the Co–10Al–5Mo–2Nb alloy. The details regarding phase stability and the effect of Ni and Ti on prolonged aging of these alloys are not available. The article reports changes that occur due to addition of Ni and Ti to this alloy including the stability at higher temperatures between 800 and 950 °C and evolution of precipitates during decomposition. The alloys studied were Co–30Ni–10Al–5Mo–2Nb and Co–30Ni–10Al–5Mo–2Nb–2Ti.

Materials and methods

Alloy buttons (30 grams) of nominal composition (in atomic%) Co–10Al–5Mo–2Nb, Co30Ni–10Al–5Mo–2Nb, and Co–30Ni–10Al–5Mo–2Nb–2Ti were prepared using a laboratory-scale vacuum arc melting unit equipped with a water-cooled copper hearth and W electrode. The constituent elements were 99.99 % pure (supplied from Alfa Aesar) and melted under argon atmosphere. Prior to melting, the chamber was evacuated to the order of $\sim 10^{-6}$ bar pressure using both rotary and diffusion pumps. After evacuating, the chamber was back filled with argon (99.99 % purity). For attaining homogeneity, the melting was carried out several times (10–12 times) and subsequently cast under argon atmosphere in water-cooled copper mold in the form of rods using a suction casting unit. The cast rods

were solutionised at 1300 °C for 15 h using a tubular vacuum furnace ($\sim 10^{-6}$ bar) and quenched in water to retain the supersaturation of the solutes in the matrix. The solutionised rods were sealed in quartz tube under vacuum ($\sim 10^{-6}$ bar) and aged isothermally at different temperatures and subsequently furnace cooled.

Both a scanning electron microscope (SEM, FEI ESEM) and transmission electron microscopes (TEM) were used for microstructural analysis of the samples subjected to various heat treatments. For SEM, both polished as well as etched samples were used for imaging with backscattered and secondary electron modes, respectively. Etching was carried out using SPAR etchant solution (100 ml distilled water, 100 ml HCl + 10 ml HNO_3, 0.3 ml of spar etchant). For accurate composition analysis, a field-emission-tipped electron probe microanalyser (EPMA, JEOL JXA-8530F) was used. In this case, only polished samples were used for accurate analysis. For TEM sample preparation, 3 mm disks from the heat-treated samples were cut and mechanically polished to a thickness of $\sim$80 μm. The final samples were prepared using a twin-jet electro polishing unit operated between 10 and 15 V with a solution of methanol and 5 vol% perchloric acid at −30 °C.

Besides microstructure, the composition profiles across phase interfaces were obtained through EDS measurements (EDAX make, model TECNAI 12T/20T/20ST, 136-5, Octane Silicon Drift Detector (SDD series)) using a transmission electron microscope (TEM) equipped with a field emission source (FEI F30 with STEM nanoprobe facility). The EDS measurements were carried out (averaging $\sim$20 EDS spectra for each reported composition) in the STEM configuration using a probe size of approximately 1 nm and the TIA (TEM imaging and analysis, FEI supply) software was used in mixed mode for quantification. The quantification was carried out using the standard library. This accuracy of the library was cross-verified in a routine manner from time to time and against results of EPMA measurements. The phase identification and orientation relationships between the phases were obtained through the selected area diffraction technique using a conventional transmission electron microscope (JEOL 2000FX). Identification of crystal structures for the phases evolved has been done by generating and comparing the reference diffraction patterns simulated using JEMS software (P. A. Stadelmann. JEMS—EMS java version, 2004) with the experimentally obtained diffraction patterns.

The solvus temperatures of the aged samples were determined by carrying out thermal analysis using a differential scanning calorimeter (DSC, NETSCH make, STA449F3) operated under argon atmosphere using a heating rate of 10 °C min^{-1}. The volume fractions of γ′ precipitates for the aged alloys were measured according to ASTM standard E562-11 [30].

Results and discussion

The microstructures of the cast samples as well as those obtained after solutionising heat treatment have been discussed in detail elsewhere [27]. After solutionising, the alloys exhibit disordered fcc γ-Co solid solution. Figure 1a and b shows the dark-field micrographs of the alloy Co–10Al–5Mo–2Nb peak aged at 800 °C for 2 h and the alloy Co–30Ni–10Al–5Mo–2Nb peak aged at the same temperature for 5 h, respectively. The images were taken near the [001] zone axis of the matrix (respective diffraction patterns are shown as insets) using 100 superlattice reflections. In both cases, γ′ precipitates exhibit cuboidal morphology. However, a significantly higher volume fraction of γ′ precipitates of around 76 % could be seen in the Ni-containing alloy compared to the Co–10Al–5Mo–2Nb alloy that contains 52 % volume fraction of γ′. The detailed microstructural analysis and mechanical properties of these alloys after aging are reported in our earlier article and have also been shown briefly in Table 1 [27].

The aging curves at 800 °C show a decrease in the hardness of the base Co–10Al–5Mo–2Nb alloy with time while there is no effect on the Co–30Ni–10Al–5Mo–2Nb alloy up to an aging time of 100 h. The solvus temperatures for the Co–10Al–5Mo–2Nb and Co–30Ni–10Al–5Mo–2Nb alloys are 866 °C and 990 °C, respectively [26, 27].

Microstructural changes in Co–10Al–5Mo–2Nb after extended exposure at 800 °C

In this section, the microstructural changes in the Co–10Al–5Mo–2Nb alloy while aging at 800 °C for extended periods have been presented and discussed. Figure 2 shows backscattered SEM images of the base alloy (Co–10Al–5Mo–2Nb) after aging at 800 °C for 35 h. The low magnification micrograph shows appearance of needle-type precipitates at the grain

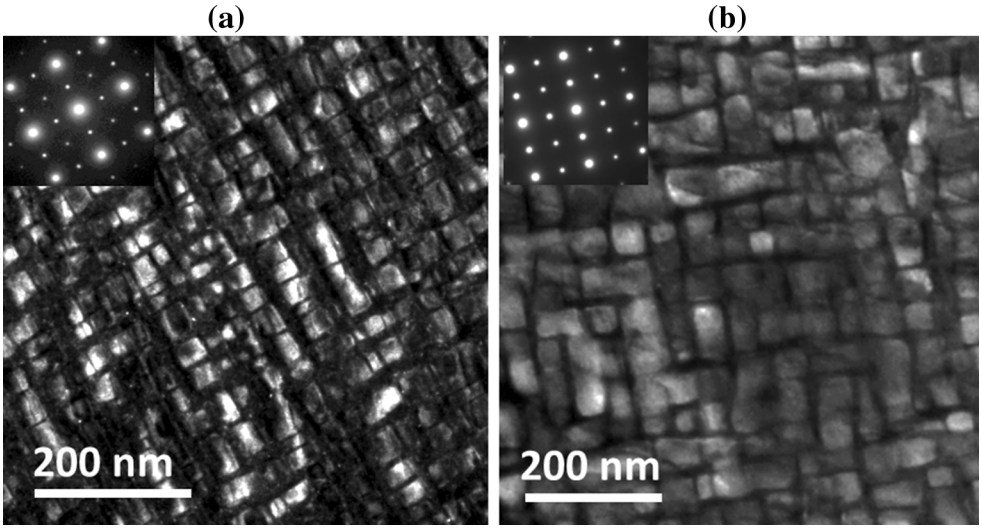

Figure 1 Dark-field micrographs taken near to the [001] matrix zone axis using the 100 super lattice reflection for **a** Co–10Al–5Mo–2Nb alloy peak aged at 800 °C, 2 h and for **b** Co–30Ni–10Al–5Mo–2Nb alloy peak aged at 800 °C, 5 h.

Table 1 Properties of Co–10Al–5Mo–2Nb and Co–30Ni–10Al–5Mo–2Nb (CoNi30) alloys [27]

Alloys	Solvus temperature (°C)	Density (gm cm^{-3})	Tensile Properties			
			0.2 % PS (MPa)	UTS (MPa)	% El	Specific 0.2 % PS (MPa/gm cm^{-3})
Co–10Al–5Mo–2Nb	866	8.36	720	835	19	86.1
CoNi30	990	8.38	790	890	17	94.3
CoNi30	870	8.38	535	575	17	62.7

boundaries as well as inside the grains in a non-uniformly distributed manner along with the γ′ precipitates in the matrix. In addition, a cellular-like growth involving three phases originating from the grain boundary and growing into the γ matrix that contains a uniform distribution of γ′ phase can be observed. These features could be seen throughout the sample.

The nature of the growth of needle-shaped precipitates has been evaluated with the help of electron microscopy. Figure 3a shows a typical micrograph using STEM HAADF technique from a region where the needle precipitates are present. The compositional EDS map (see supplementary figure S1) and profile scan (Fig. 3b) indicate that these precipitates are mainly rich in Mo and Nb. The measured overall compositions of these precipitates are Co–0.7Al–12.3Mo–11.8Nb which is close to the stoichiometry of Co_3(Mo, Nb). It can be noted that most of the Al atoms partition into the fcc γ-Co matrix. The crystal structure of the needles and the orientation relationship with the γ matrix could be established through diffraction analysis. Figure 3c shows a diffraction pattern taken along [011] matrix zone axis from a region that contains needle-shaped precipitates. The main reflections belong to fcc γ-Co while the superlattice spots could be indexed as the DO_{19} structure that corresponds to the Co_3(Mo, Nb) needle precipitates. Along with these, one can also observe weak superlattice spots in between the transmitted beam and 200 type of matrix reflections. These weak spots appear due to the presence of $L1_2$-ordered precipitates in the nearby matrix region. The schematic of the indexed pattern is also included in Fig. 3c. The orientation relationship between the ordered Co_3(Mo, Nb) phase and the fcc γ-Co phase was found to be

$$\begin{matrix}[1\bar{2}10]_{Co_3(Mo,Nb)} || [011]_{\gamma-Co} \\ (0001)_{Co_3(Mo,Nb)} || (11\bar{1})_{\gamma-Co}\end{matrix} . \quad (1)$$

The needle precipitates are however not stable. A careful observation shows nucleation of a second phase that consumes a portion of the needle. This is

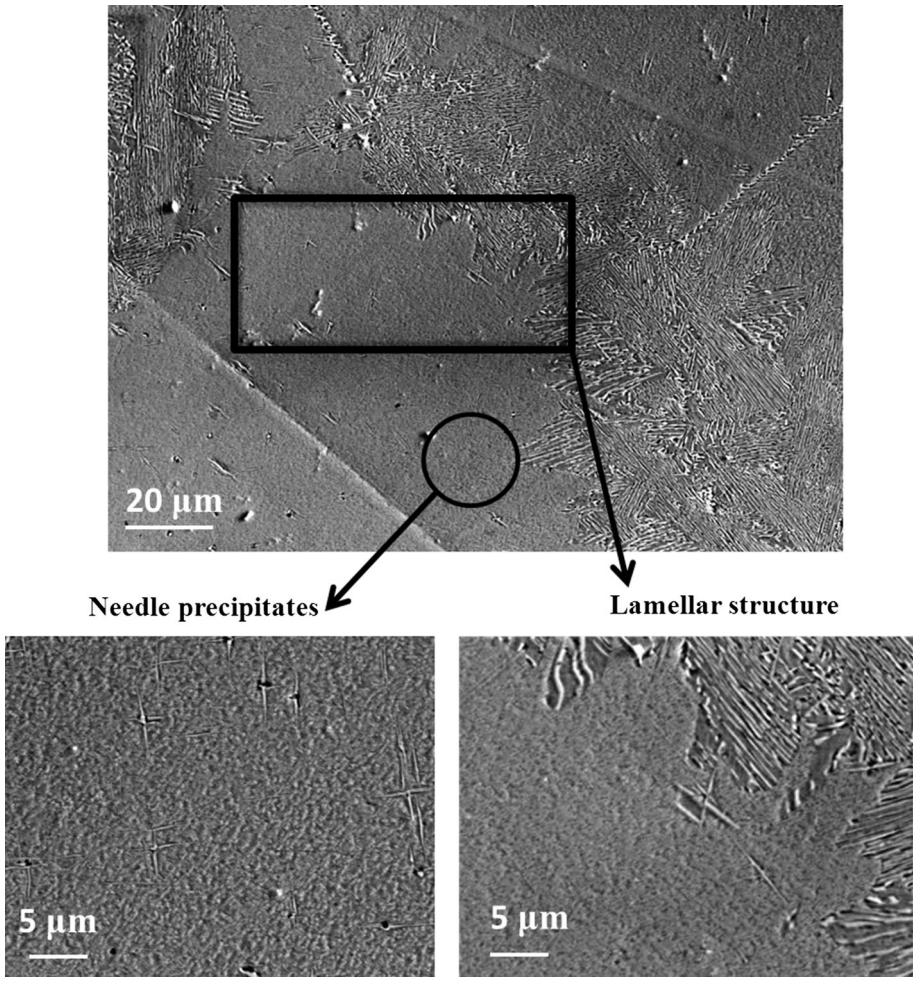

Figure 2 Backscattered SEM images of the base alloy Co–10Al–5Mo–2Nb after aging at 800 °C for 35 h showing needle precipitates inside the grains and two-phase cellular growth from the grain boundary toward the grain interior.

shown in the inset of Fig. 3a. The structure of this phase is presented later.

As mentioned earlier, the microstructural observations suggest that in addition to needle precipitates, phases with cellular morphology develop from the grain boundaries. Figure 4a shows a STEM HAADF micrograph that exhibits the cellular decomposition products with an interface separating the three-phase cellular colony from the γ matrix. There exist two types of lamellar contrast (one darker and the other comparatively lighter) coexisting in the cell. The EDS elemental mapping [see supplementary S2(a)] indicates the phase with dark contrast to be Al-rich, while the brighter one is rich in Mo and Nb. The compositions of the respective phases are given in Table 2. The phase with darker contrast has the composition Co–29.3Al–0.4Mo–0.7Nb while composition of the brighter phase is Co–0.6Al–11.5Mo–8.7Nb that is close to the stoichiometry $Co_{79}(Mo, Nb)_{21}$. The region separating the lamellae inside the cell (gray contrast) is a Co-rich solid solution (γ1). The EDS measurement using STEM nanoprobe indicates the composition to be Co–3.2Al–3.1Mo–0.7Nb. In contrast, the original composition of the γ matrix located at the other side of the cellular interface is Co–4.2Al–4.4Mo–1.5Nb. The results indicate significant reduction of solute concentrations in the γ phase located at cellular regions compared to the original matrix. This is consistent with the general characteristic of cellular decomposition.

The crystal structure of the coexisting phases during decomposition and their orientations relationships were determined through diffraction analysis. Figure 4b shows a diffraction pattern taken along the [112] zone axis of the Co matrix. The reflections could be indexed as fcc γ_1-Co. Along with these fcc reflections, additional spots were present. These can be indexed as reflections from a B2-ordered phase and reflections from a DO_{19}-ordered phase. The schematics detailing the indexing of coexisting

patterns are also presented in the same figure. Figure 4c, d show the dark-field micrographs taken from the respective superlattice spots of B2 and DO_{19} phases [a low magnification bright-field micrograph is also shown in supplementary S2(b)]. The micrograph shown in Fig. 4c was taken from the $\bar{1}\bar{2}1$ spot of B2 phase near the [113] zone axis while Fig. 4d was taken from the $\bar{1}2\bar{1}0$ spot of the DO_{19} phase near the $[10\bar{1}0]$ zone axis. A comparison of Fig. 4a, c, and d establishes a three-phase coexistence of B2, DO_{19}, and $\gamma 1$ in the cellular region. We note that in the diffraction pattern, there is no signature of $L1_2$ ordering. This suggests that these phases are formed at the expense of γ'-ordered precipitates. The orientation relationship of these phases were found to be

Figure 4 **a** STEM HAADF image of the lamellar region in the base Co–10Al–5Mo–2Nb alloy after 35 h of aging at 800 °C. **b** Diffraction pattern taken from the lamellar region imaged along the [112] zone axis of the fcc γ-Co matrix containing reflections from two other phases (B2 CoAl and DO_{19} Co_3(Mo, Nb)) and schematic indexed pattern. **c** Dark-field micrographs taken from the $\bar{1}\bar{2}1$ reflection of the B2 CoAl phase and **d** superlattice reflection of the DO_{19} phase. **e** EDS Profile line scan across the interface between the γ and (*i*) DO_{19} Co_3(Mo, Nb) bright phase (*ii*) B2 CoAl dark phase, and (*iii*) Co solid solution (γ_1).

$$\begin{matrix}[\bar{1}\bar{1}1]_{\gamma-Co}||[1\bar{1}0]_{B2-CoAl}||[000\bar{1}]_{DO_{19}-Co_3(Mo,Nb)} \\ (101)_{\gamma-Co}||(111)_{B2-CoAl}||(11\bar{2}0)_{DO_{19}-Co_3(Mo,Nb)}\end{matrix} . \quad (2)$$

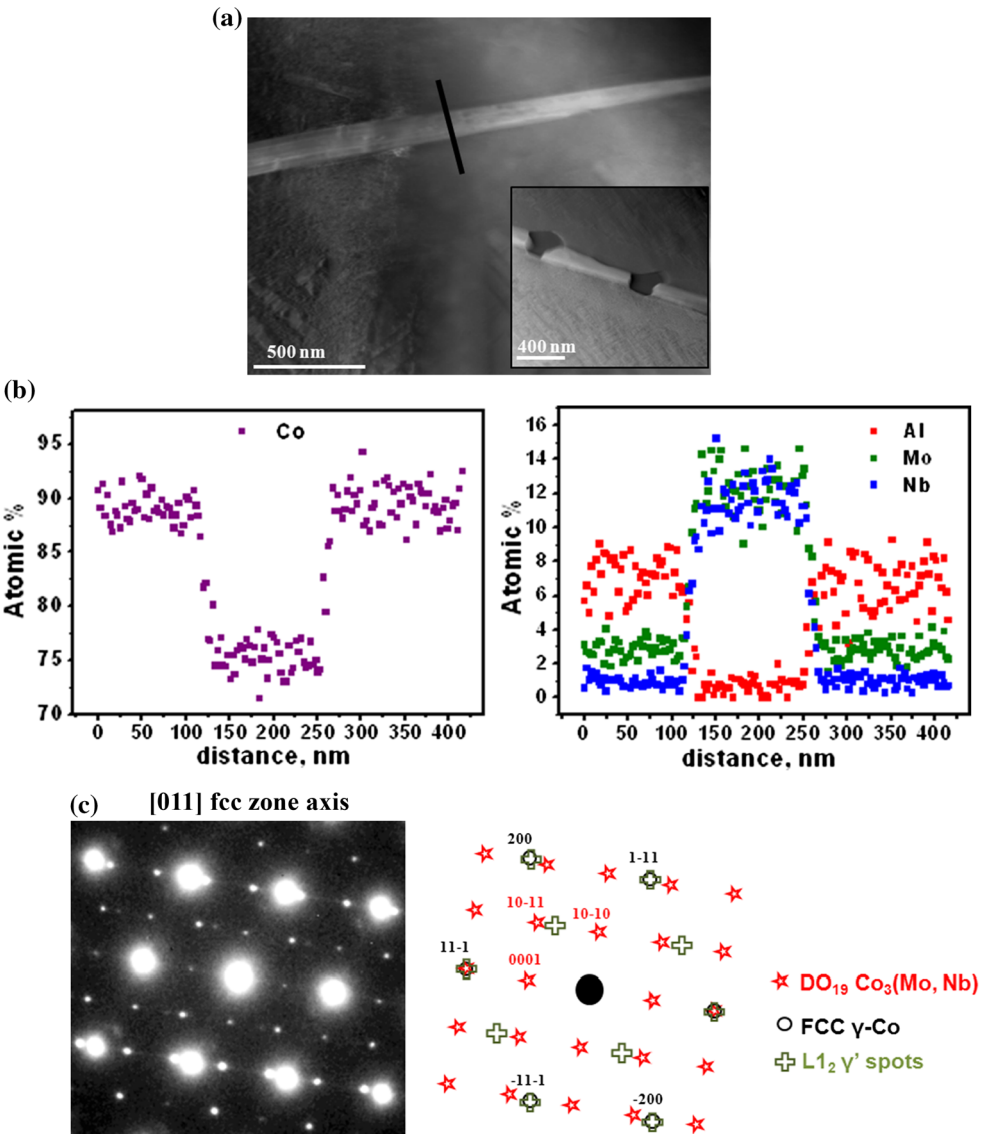

Figure 3 **a** STEM HAADF image showing a needle-shaped precipitate in the Co–10Al–5Mo–2Nb alloy aged at 800 °C for 35 h. **b** EDS elemental line scan across the needle precipitate using STEM nanoprobe **c** and the diffraction pattern taken parallel to the [011] matrix zone axis from the region containing the needle precipitate with a schematic of indexed pattern.

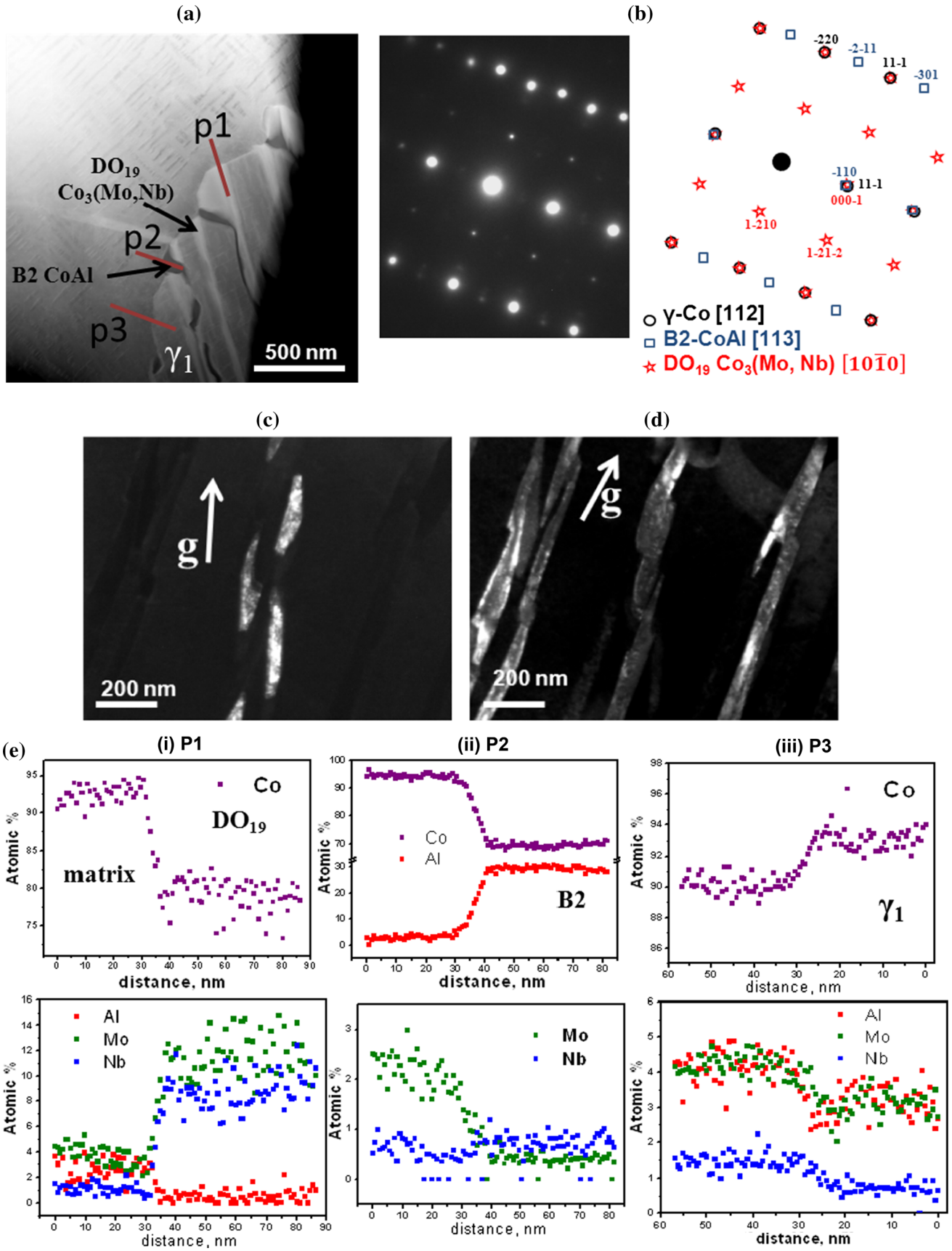
(a)
p1
DO19
Co3(Mo,Nb)
p2
B2 CoAl
p3
γ1
500 nm
(b)
-220
-2-11
11-1
-301
-110
11-1
000-1
1-210
1-21-2
γ-Co [112]
B2-CoAl [113]
DO19 Co3(Mo, Nb) [10$\bar{1}$0]
(c)
g
200 nm
(d)
g
200 nm
(e)
(i) P1
Co
DO19
matrix
Atomic %
distance, nm
(ii) P2
Co
Al
B2
Atomic %
distance, nm
(iii) P3
Co
γ1
Atomic %
distance, nm
Al
Mo
Nb
Atomic %
distance, nm
Mo
Nb
Atomic %
distance, nm
Al
Mo
Nb
Atomic %
distance, nm

Table 2 EDS compositions measured using STEM nanoprobe of the phases that appears during 35 h of aging in the Co–10Al–5Mo–2Nb alloy at 800 °C

Co–10Al–5Mo–2Nb aged at 800 °C for 35 h	Constituent elements (at.%)			
	Co	Al	Mo	Nb
Needle precipitate [DO_{19} Co_3(Mo, Nb)]	75.2 ± 0.6	0.7 ± 0.2	12.3 ± 0.4	11.8 ± 0.3
Dark phase (B2 CoAl)	69.7 ± 0.7	29.4 ± 0.5	0.4 ± 0.2	0.7 ± 0.3
Bright phase [DO_{19} Co_3(Mo, Nb)]	79.2 ± 0.5	0.6 ± 0.2	11.5 ± 0.5	8.7 ± 0.6
Solute-depleted Co solid solution (γ_1)	93 ± 0.7	3.2 ± 0.4	3.1 ± 0.3	0.7 ± 0.2
Solid solution (γ)—P1	94.6 ± 0.6	2.3 ± 0.3	2.3 ± 0.2	0.8 ± 0.1
Solid solution (γ)—P2	92.6 ± 0.6	2.6 ± 0.2	3.6 ± 0.3	1.2 ± 0.2
Solid solution (γ)—P3	89.9 ± 0.6	4.2 ± 0.3	4.4 ± 0.2	1.5 ± 0.1

The fcc γ-Co and B2 phases follow Kurdjumov–Sachs (KS) orientation relationship while DO_{19} phase has Burgers orientation relation with γ-Co. The orientations of these three phases are shown using the stereographic projection in Fig. 5.

To determine the compositional changes across the boundary, the EDS profiles were taken using STEM nanoprobe. The results are summarized in Table 2. The phase with B2 structure is rich in Al having the composition $Co_{70}Al_{30}$ with marginal partitioning of Mo and Nb. This suggests that the B2 phase is non-stoichiometric similarly to the NiAl phase. The composition of DO_{19} phase with brighter contrast corresponds to Co_3(Mo, Nb). The composition profiles of the three phases across the cell boundaries are shown in Fig. 4e. The solute variations across the phase boundary (lines P1, P2, and P3) are from the region (i) DO_{19} Co_3(Mo, Nb), (ii) B2-CoAl, and (iii) γ_1-Co to the γ-Co matrix, respectively. Local compositions of the γ matrix near the respective interfaces (P1, P2, and P3) are shown in Table 2.

The present study establishes that the cuboidal $L1_2$-ordered γ′ precipitates are metastable in the Co–10Al–5Mo–2Nb alloy at 800 °C and thus the measured solvus temperature (i.e., 866 °C) through DSC is a metastable solvus temperature. The decomposition occurs via two routes. The first being the direct precipitation in the grain interior of DO_{19} Co_3(Mo, Nb) phase in the form of Widmanstäten needles. However, accumulation of Al at the interface leads to the nucleation of the B2 phase.

The second mode is a unique cellular precipitation where a cellular front grows from grain boundary to the grain interior that contains γ′ precipitates in the γ matrix. The front consists of alternating layers of γ solid solution and lamellae of DO_{19} Co_3(Mo, Nb) and B2 CoAl. Cellular precipitation originating from grain boundaries is well known [31, 32]. There exist detailed studies of cellular precipitation consuming a matrix containing precipitates in Al–Zn alloys which resembles what is being observed in the present case [33–38]. It is to be noted that diffusion couple experiments in Co–Al–W alloys at 900 °C have shown that the $L1_2$-ordered Co_3(Al, W) phase is metastable and decomposes into equilibrium phases consisting of fcc γ, B2 CoAl, and DO_{19} Co_3W [39, 40]. This is generally described in the literature as eutectoid-like decomposition. However, the present observation is unique as described below.

The results suggest that the decomposition of our alloy which exhibited a two-phase γ–γ′ microstructure occurred in a cellular manner. Besides fcc γ, plates of precipitates grow normal to the cellular interface in a coordinated manner that resembles diffusion coupling across the cellular interface. However, the unique feature of the present growth is that two different phases comprise the growing plates. A careful examination of Fig. 4a reveals that two precipitates having DO_{19} Co_3(Mo, Nb) and B2 CoAl crystal structures appear sequentially in the cell with one nucleating on the other. The composition of γ across the DO_{19} Co_3(Mo, Nb) phase is enriched with Al (see P1 in Fig. 4e). The growth will continue until the local γ composition is sufficiently enriched with Al. At a certain critical enrichment level, the system will prefer nucleation and growth of the B2 CoAl phase at the Al-enriched interface between the γ and DO_{19} Co_3(Mo, Nb). Similarly, the γ composition near the P2 interface is richer in Mo and Nb than the phase B2 CoAl. As a consequence, Co_3(Mo, Nb) with DO_{19} structure will nucleate and grow when the γ composition is sufficiently enriched with Mo and Nb. Through this sequence of repeated formation of phases, the cellular growth can proceed from the grain boundary through one of the grains at the expense of original γ–γ′ microstructure. It is

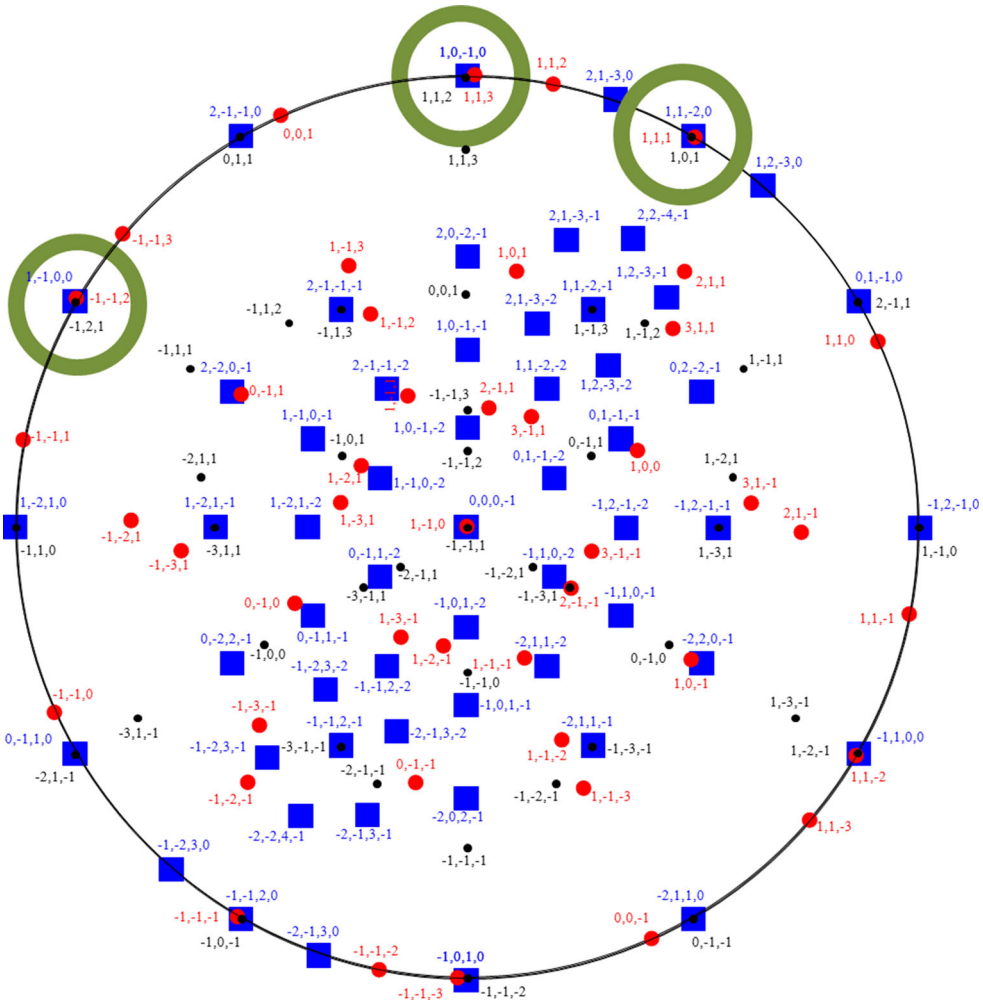

Figure 5 Schematic superposition of Stereographic projections normal to the $[\bar{1}\ \bar{1}\ 1]$ for γ_1-Co (*filled circle*), $[1\ \bar{1}\ 0]$ for B2-ordered CoAl (*filled circle*) and $[000\ \bar{1}]$ for DO_{19}-ordered $Co_3(Mo, Nb)$ (*filled square*) phases.

emphasized that although the process was termed as cellular precipitation, the process cannot be explained by the well-established growth mechanisms as elucidated by either Tu and Tunbull [41] or Fournelle and Clark [42]. The process involves diffusional growth as well as repeated heterogeneous nucleation that needs to be further explored in the future.

As discussed earlier, the three phases exhibit well-defined orientation relationships as they nucleate on each other.

Phase stability and decomposition behavior of Co–30Ni–10Al–5Mo–2Nb alloy

In an earlier article, it has been established that Ni increases the solvus temperature of the γ′ phase [27]. The microstructural stability of such alloys can be compared with the results for the base alloy presented in the earlier section. In the case of Ni-containing alloy (Co–30Ni–10Al–5Mo–2Nb), no significant change in the volume fraction and size of the γ′ precipitates could be observed after 100 h of aging at 800 °C (Fig. 6a). In comparison, $L1_2$-ordered precipitates in Co–10Al–5Mo–2Nb alloy decompose at this temperature. Since the solvus temperature of the Ni-containing alloy is 990 °C, it was aged at 900 °C for 100 h. The SEM backscattered image (Fig. 6b) shows ordered γ′ precipitates without any sign of decomposition. The precipitate size ranges from 200 to 300 nm and the volume fraction after high-temperature exposure (900 °C) is reduced to 56 from 76 %. To characterize element partitioning behavior, an EDS line scan using STEM nanoprobe was carried out across the γ′ phase and is shown in Fig. 6c. The Ni, Al, and Nb show strong partitioning to the ordered γ′ precipitates with respect to the γ-Co matrix while the concentration of molybdenum remains similar across the γ–γ′ interface. The

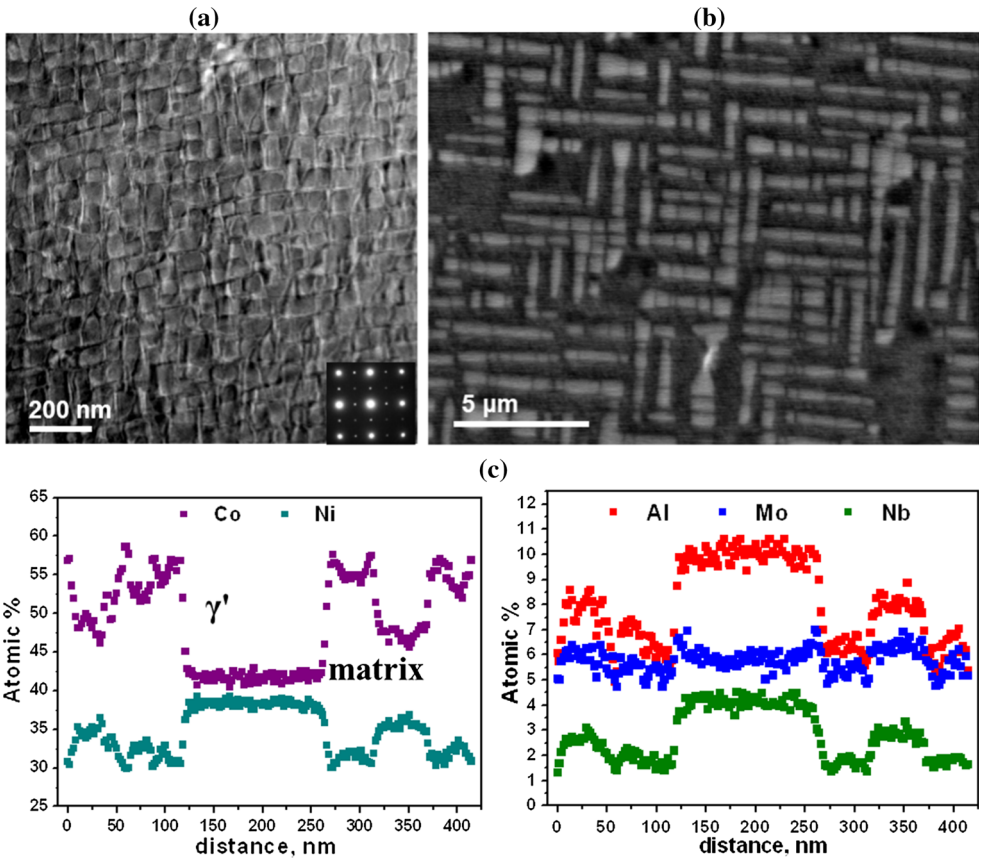

Figure 6 **a** STEM HAADF image of the $L1_2$-ordered precipitate region in the Co–30Ni–10Al–5Mo–2Nb alloy aged at 800 °C for 100 h viewed along the [001] crystallographic direction, **b** Backscattered SEM image for Co–30Ni–10Al–5Mo–2Nb alloy aged at 900 °C for 100 h, and **c** EDS elemental mapping and line scan across the γ/γ′ interfaces showing the elemental partitioning in the Co–30Ni–10Al–5Mo–2Nb alloy aged at 900 °C for 100 h.

composition of the γ′ precipitate is found to be Co–38.3Ni–10.1Al–5.8Mo–4.2Nb. Ni addition enhances the phase field area of the γ′ and hence the stability of the γ′ precipitates increases [22, 23]. The results reveal that on aging at 900 °C for 100 h, the metastable-ordered precipitate does not decompose into equilibrium phases in contrast to the base alloy composition of Co–10Al–5Mo–2Nb.

The stability of the γ–γ′ microstructure at 950 °C for 100 h, which is close to the solvus temperature of 990 °C, was also studied. Figure 7a shows a SEM backscattered image. The microstructure does not contain cuboidal precipitates. Instead, other phases appear in the microstructure. Four morphologically distinct phases can be distinguished. Some of these belong to the family of TCP phases that are detrimental for high temperature and creep properties of the superalloys [43] and are known to form during long exposures at elevated temperatures [44]. The formation and the effect of TCP phases on properties in Ni-based super alloys have been extensively studied [45–48]. The presence of these phases in the microstructure reduces the solute content in the matrix and hence reduces the solid solution strengthening contribution to the overall strength of an alloy. Precipitation of these phases at high temperatures leads to brittle fracture. This is due to the weak interfacial strength between the matrix and TCP phases and the formation of voids resulting in interfacial de-cohesion upon the application of load [45, 49]. The compositions of all the phases have been determined using STEM nanoprobe EDS measurements and shown in Table 3.

A1 is a Mo-rich phase with the composition Co–4.2Ni–14Al–70.9Mo–5.7Nb. Figure 7b shows a bright-field micrograph and the diffraction pattern taken from the phase. The pattern is indexed as the TCP1 phase which has the A15 crystal structure with the [103] zone axis aligned parallel to the optical axis of the TEM. The space group of this phase is classified as $pm\bar{3}n$. The dark-field image from the 020 spot confirms the identity of the A1 phase. Figure 8a shows a bright-field micrograph of the needle precipitate that has two types of contrasts. The compositions of these two phases were measured and found to be different (Table 3). They were named A2 and A3, respectively.

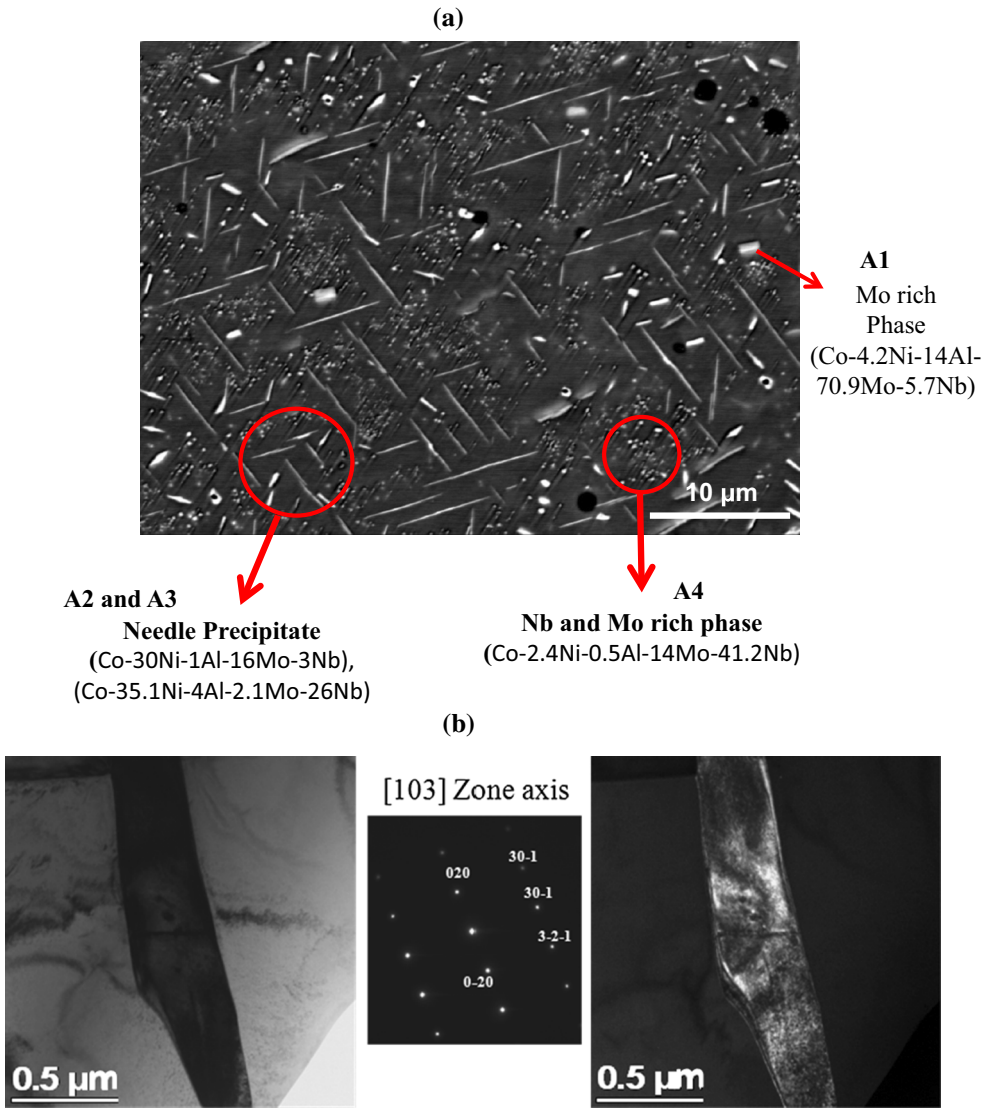

Figure 7 **a** Backscattered SEM images of the Co–30Ni–10Al–5Mo–2Nb alloy aged at 950 °C for 100 h showing TCP phases in the microstructure and their compositions. **b** A pair of bright-field and dark-field micrographs taken along [103] zone axis of the Mo-rich A1 phase present in the matrix. The diffraction pattern is matched to the A15 crystal structure with the space group pm-3n with the lattice parameter $a = 0.4951$ nm.

A2 comprises mainly of Co, Ni, and Mo, while A3 has Co, Ni, Al, and Nb. The diffraction pattern taken along the [101] matrix zone axis contains extra spots along with the fundamental reflections. These spots arise due to the presence of two different phases. The nets corresponding to these phases are outlined on the diffraction pattern. Both the nets correspond to hexagonal crystal structures, but have different lattice parameters. The crystal symmetry of the phase A2 is characterized by the $P6_3/mmc$ space group with lattice parameters 'a' and 'c' equal to 0.285 and 0.462 nm, respectively. Similarly, the A3 crystal symmetry is described by the same space group but with larger lattice parameters ('a' and 'c' equal to 0.421 and 0.682 nm, respectively). This phase can be categorized as the Laves phase (TCP2 phase) with a prototype structure analogous to $MgZn_2$. A schematic of the indexed pattern is shown in Fig. 8a and also the simulated reference patterns were shown in supplementary information S3(c) for γCo/A2 and (d) γCo/A3, respectively. Both the phases have specific orientation relationships with the γ matrix. These can be expressed as

Table 3 EDS compositions taken using STEM nanoprobe of all the phases present in Co–30Ni–10Al–5Mo–2Nb alloy aged at 950 °C for 100 h

	Composition (at.%)					Crystal structure	Prototype	Space group	Lattice parameter
	Co	Ni	Al	Mo	Nb				
A1	5.2 ± 0.2	4.2 ± 0.3	14 ± 0.3	70.9 ± 0.5	5.7 ± 0.2	Cubic A15 crystal structure	Cr_3Si [50]	Pm-3n	$a = b = c = 0.465$ nm
TCP1									
A2	50 ± 0.1	30 ± 0.2	1 ± 0.2	16 ± 0.6	3 ± 0.3	Hexagonal	Mg [51]	$P6_3/mmc$	$a = b = 0.285$ nm and $c = 0.463$ nm
A3	32.8 ± 0.1	35.1 ± 0.2	4 ± 0.3	2.1 ± 0.4	26 ± 0.6	Hexagonal (Laves phase)	$MgZn_2$ [52]	$P6_3/mmc$	$a = b = 0.421$ nm and $c = 0.682$ nm
TCP2									
A4	42.8 ± 0.3	2.4 ± 0.3	0.5 ± 0.2	14 ± 0.5	41.2 ± 0.4	Rhombohedral (μ phase)	W_6Fe_7 [53]	R-3m	$a = b = 0.4904$ nm and $c = 2.618$ nm, $\beta = 120°$
TCP3									

$$[101]_{\gamma-Co}||[2\bar{1}\bar{1}0]_{A2}||[20\bar{2}1]_{A3(TCP2)}$$
$$(\bar{1}11)_{\gamma-Co}||(0001)_{A2}||(0\bar{1}12)_{A3(TCP2)} \quad (3)$$

These two phases can be distinguished easily by taking dark-field micrographs from the respective phase reflections present in the diffraction pattern. Figure 8b shows dark-field images taken using the $01\bar{1}0$ A2 reflection and the $\bar{1}102$ A3 reflection, respectively.

Figure 9a shows a bright-field micrograph of a region containing a phase (A4) with distorted cuboidal morphology. The diffraction pattern taken along the [101] matrix zone axis shows double diffraction spots along with the main reflections. Hence, to distinguish the A4 phase reflections, microdiffraction patterns were taken from both the A4 and the nearby matrix region and shown in the same figure. The A4 phase was identified as μ phase (TCP3) which has a rhombohedral crystal structure. The lattice parameters 'a' and 'b' have values of 0.4904 and 2.618 nm, respectively.

The schematic indexing of the pattern is shown in Fig. 9b and the simulated reference pattern is also shown in supplementary information S4(c) for γCo/A4. The composition and the prototype structure are presented in Table 3. The orientation relationship of this phase with the matrix can be expressed as

$$(020)_{\gamma-Co}||(2\bar{1}\bar{1}6)_{A4(TCP3)}$$
$$(\bar{1}01)_{\gamma-Co}||(0\bar{1}10)_{A4(TCP3)} \quad (4)$$

There are very few reports on phase decomposition and TCP phase formation in γ–γ′ Co-based superalloys when exposed to high temperatures. The most detailed work to date is that of Yan et al. [6, 7] which has studied a large number of alloys with quaternary additions to a base Co–Al–W alloy. Existence of three secondary phases was reported: a DO_{19}-ordered χ phase of essentially Co_3W composition, B2-ordered β phase of CoAl composition, and occasionally μ phase with a rhombohedral crystal structure. The μ phase has a general composition of Co_7W_6. However, this is stabilized by other alloying additions as well. The presence of these three phases in the Co–Al–W system has also been shown by diffusion couple experiment [39, 40]. In Ni-based γ–γ′ alloys, the most commonly observed TCP phases are σ (tetragonal), P (orthorhombic), μ (rhombohedral), and R phase. The σ phase often forms first and acts as a site for second-phase nucleation [54]. The orientations of these

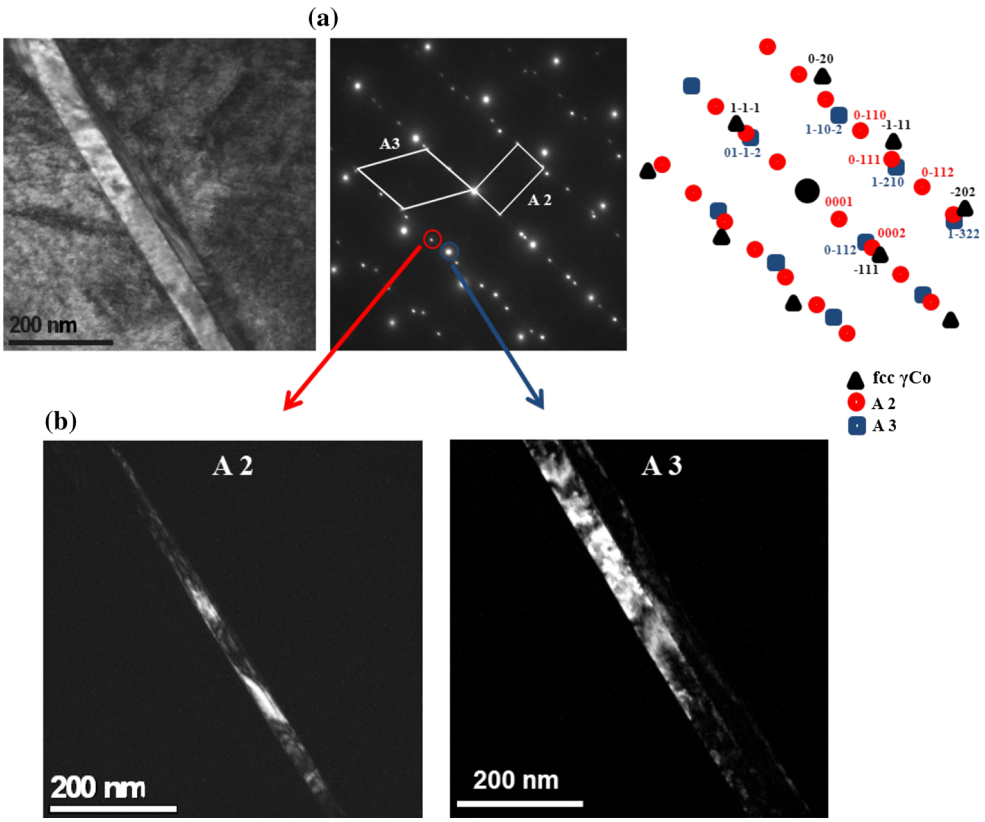

Figure 8 **a** A bright-field micrograph showing the needle-shaped phase with two different contrasts taken near the [101] matrix zone axis. The diffraction pattern shows spots from two different hexagonal phases with a particular orientation relationship (see schematic indexed pattern). **b** Dark-field micrographs taken from the $01\bar{1}0$ spot of the A2 phase and from the $\bar{1}102$ spot of the A3 phase.

phases with the matrix and their morphologies were studied extensively [55–58]. However, the σ and P phases are yet to be observed both in our alloys as well as in Co–Al–W alloys.

We now discuss the composition of the secondary phase observed in this work. The phase identified as TCP1 is of Cr_3Si type and has cubic A15 structure. This phase has a general stoichiometry of A_3B with A and B atoms occupying distinct sites resulting in an ordered structure. In our case, the A sites have CN14 coordination and are most likely occupied by Mo and Nb while B sites (CN12) are occupied by Al, Co, and Ni in that order. In contrast, the TCP2 phase is a hexagonal Laves phases of $MgZn_2$ type. The axial ratio is 1.62 which is slightly less than the ideal value of 1.633. The observed stoichiometry is close to AB_2 with Nb atoms together with small amount of Al and Mo occupying the A sites while Co and Ni almost equally occupying the B sites in the structure.

The third TCP phase observed is the μ phase which has a rhombohedral structure with a stoichiometry of A_7B_6. This phase also appears in the Co–Al–W alloy. The isotype of this phase is Fe_7W_6. However, our composition analysis suggests that Nb and a smaller amount of Mo most likely occupy the B sites while Co and Ni occupy the A sites. One therefore needs to verify the exact composition by other techniques to confirm this finding.

The occurrence of hcp solid solution of Co (A2 phase) as a decomposition product in our alloys needs special mention. This solid solution contains very little of Al and Mo and predominantly coexists with Laves phase that also contain very little Al. The A1 precipitate is the only one which predominantly contains Mo and to a lesser extent Al compared to γ matrix. Thus, the precipitation of TCP 1 is crucial for the precipitation of other phases.

We must add that similarly to the observations in the Co–Al–W alloys [7, 39], we have also observed the ordered DO_{19} phase as well as the B2 CoAl phase in the base Co–10Al–5Mo–2Nb alloy. However, we show that at least in our case, the decomposition does not follow a eutectoid reaction. With Ni as an alloying addition, the decomposition pathway shifts to yield the TCP phases.

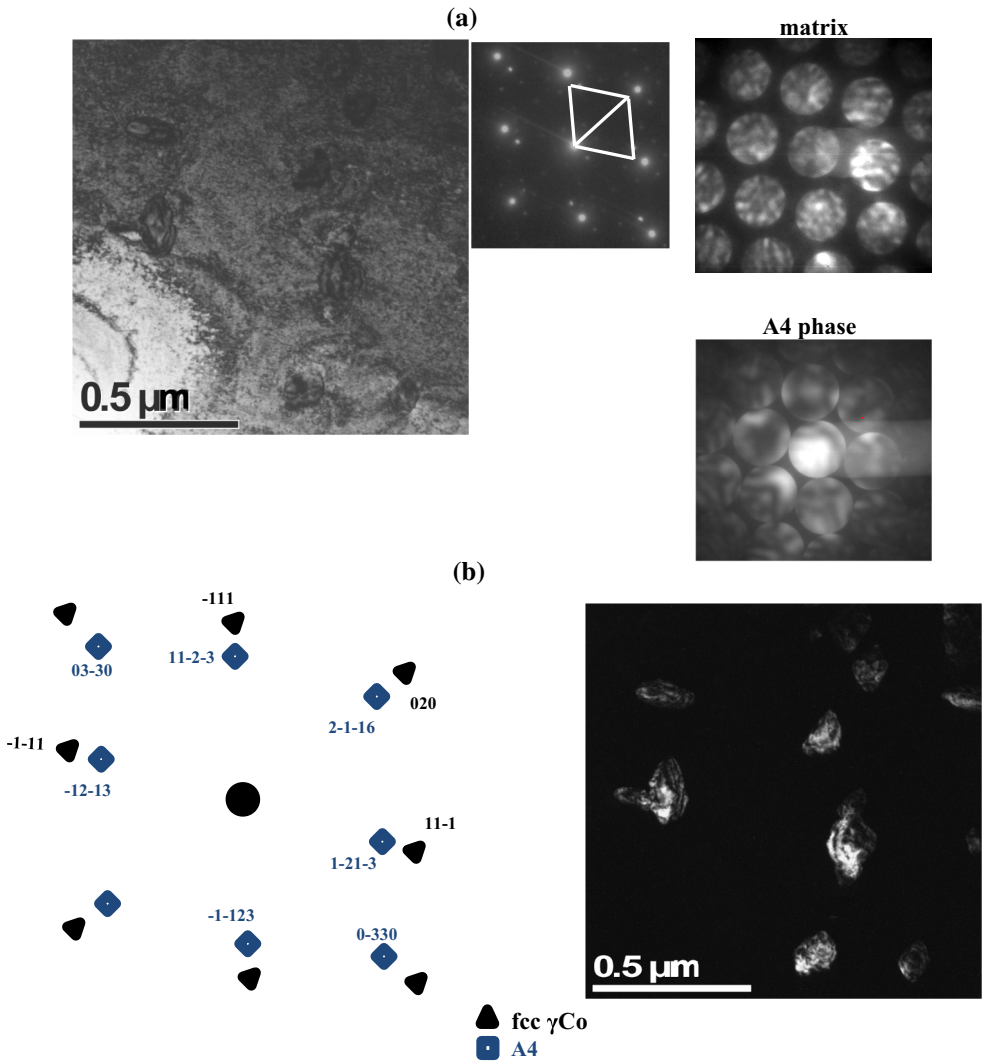

Figure 9 A bright-field image showing the TCP 4 phase taken along the [101] matrix zone axis and diffraction pattern showing spots that were indexed as the rhombohedral (μ phase) structure (see schematic indexed pattern). **b** The dark-field micrograph taken using the $11\bar{2}\,\bar{3}$ spot reflects the A4 phase present in the matrix.

Stability of Co–30Ni–10Al–5Mo–2Nb–2Ti alloy

To increase the solvus temperature further, 2 at.% Ti is added to the Ni-containing alloy. It is shown in earlier reports that Ti is a strong γ′ stabilizer and hence addition in small amounts increases the solvus temperature significantly [12, 14]. The solvus temperature of the Co–30Ni–10Al–5Mo–2Nb–2Ti alloy was found to be 1030 °C that is greater than the solvus of other two alloys (Fig. 10a). To check the stability of this alloy at 950 °C, the solutionised samples were aged at 950 °C. Figure 10b shows the SEM backscattered image of the aged sample. It contains γ-γ′ microstructure with the precipitate sizes ranging from 400 to 800 nm. Neither decomposition of γ–γ′ nor TCP phases were observed after 100 h of aging 950 °C. However, the microstructure shows directional coarsening (rafting, coalescence of γ′ cuboidal precipitates in one direction) of γ′ precipitates that can be attributed to high misfit strain across γ/γ′, high volume fraction, and high temperature of aging. In operational conditions, on application of low stresses at high temperatures, rafted microstructure resists creep but at high temperatures it accelerates creep [59]. In the present alloys, the lattice misfit can be altered by addition of Cr and thus the directional coarsening can be avoided during aging [60].

Conclusion

The present work explores the nature of the stability of the $L1_2$-ordered Co_3(Al, Mo, Nb) phase in the newly discovered Co–10Al–5Mo–2Nb alloy. On

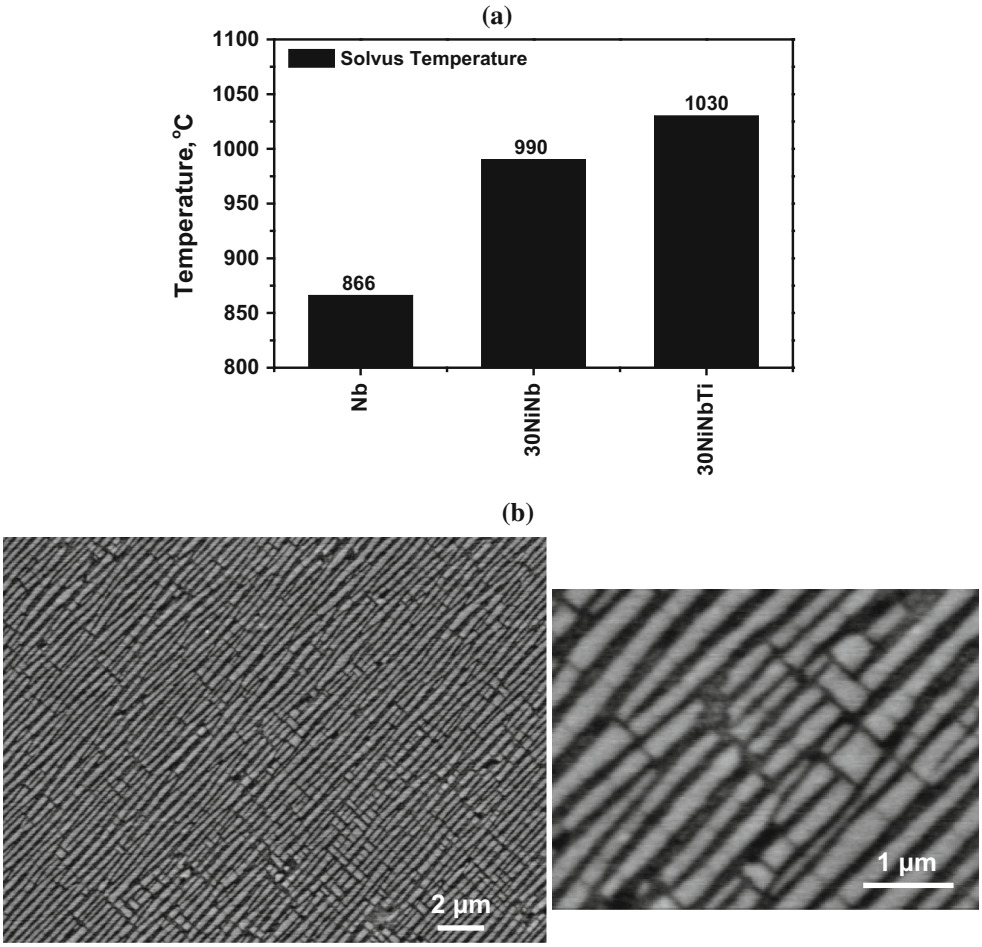

Figure 10 **a** Comparison of the solvus temperatures of base Co–10Al–5Mo–2Nb (Nb), Co–30Ni–10Al–5Mo–2Nb (30NiNb), and Co–30Ni–10Al–5Mo–2Nb–2Ti (30NiNbTi) alloys. **b** Backscattered SEM image of the Co–30Ni–10Al–5Mo–2Nb–2Ti alloy after aging at 950 °C for 100 h showing no sign of decomposition or TCP phase formation.

aging at 800 °C for 35 h, needle-type precipitates of Co_3(Mo, Nb) with DO_{19}-ordered structure appear in the microstructure. The $L1_2$-ordered phase is therefore metastable and on decomposition yields three equilibrium phases which include fcc γ_1-Co, B2 CoAl, and DO_{19} Co_3(Mo, Nb) with specific orientation relationships with one another. Morphology similar to those observed during cellular precipitation could also be observed during the decomposition process. However, the evolution of the three phases is more complex and most likely aided by repeated heterogeneous nucleation of the phases on one other.

It can be concluded that microstructural stability and resistance to decomposition is influenced by the solvus temperature. With substitution of some part of Co (~30 at.%) in Co–10Al–5Mo–2Nb alloy with Ni (solvus temperature 990 °C), the decomposition of the ordered metastable $L1_2$ phase can be suppressed up to 900 °C. However, when aged at 950 °C that is close to the solvus temperature, TCP phases appear in the microstructure. Detailed crystallographic characterization of these phases reveals four phases that can be distinguished in terms of chemistry and crystallography. The γ–γ' microstructure in the Co–10Al–5Mo–2Nb and Co–30Ni–10Al–5Mo–2Ta alloys is not stable at 800 and 950 °C, respectively, that shows the measured solvus temperatures (i.e., 866 and 990 °C) are metastable solvus temperatures. With addition of 2 % Ti to the Co–30Ni–10Al–5Mo alloy, the metastable solvus temperature can be further increased to 1030 °C. This alloy still retains a two-phase γ–γ' microstructure when aged at 950 °C for 100 h without any decomposition or formation of TCP phases.

Acknowledgements

All the authors would like to acknowledge the microscope facility available at Advanced Facility for

Microscopy and Microanalysis (AFMM) center, Indian Institute of Science, Bangalore. One of the authors acknowledges the financial support from department of science and technology in the form of J.C. Bose national fellowship. All the authors acknowledge the discussion and support from Professor Dipankar Banerjee and Professor Subodh Kumar.

Compliance with ethical standards

Conflict of interest The authors declare that have no conflicts of interests.

Electronic supplementary material: The online version of this article (doi:10.1007/s10853-016-0026-1) contains supplementary material, which is available to authorized users.

References

[1] Suzuki A, DeNolf GC, Pollock TM (2007) Flow stress anomalies in γ/γ' two-phase Co–Al–W-base alloys. Scr Mater 56:385–388

[2] Xue F, Zhou HJ, Feng Q et al (2015) Creep behavior in a γ' strengthened Co–Al–W–Ta–Ti single-crystal alloy at 1000 °C. Scr Mater 97:37–40

[3] Suzuki A, Pollock TM (2008) High-temperature strength and deformation of γ/γ' two-phase Co–Al–W-base alloys. Acta Mater 56:1288–1297

[4] Inui H, Oohashi T, Okamoto NL et al (2011) Physical and mechanical properties of $Co_3(Al, W)$ with the L12 structure in single and polycrystalline forms. Key Eng Mater 465:9–14

[5] Klein L, Shen Y, Killian MS, Virtanen S (2011) Effect of B and Cr on the high temperature oxidation behaviour of novel γ/γ'-strengthened Co-base superalloys. Corros Sci 53:2713–2720

[6] Yan H-Y, Vorontsov VA, Dye D (2014) Alloying effects in polycrystalline γ' strengthened Co–Al–W base alloys. Intermetallics 48:44–53

[7] Yan H-Y, Coakley J, Vorontsov VA et al (2014) Alloying and the micromechanics of Co–Al–W–X quaternary alloys. Mater Sci Eng, A 613:201–208

[8] Meher S, Yan H-Y, Nag S, Dye D, Banerjee R (2012) Solute partitioning and site preference in γ/γ' Cobalt base alloys. Scr Mater 67:850–853

[9] Lee CS (1971) Precipitation-hardening characteristics of ternary Co–aluminum-X alloys. PhD Dissertation, University of Arizona

[10] Sato J, Omori T, Oikawa K et al (2006) Co-base high-temperature alloys. Science 312:90–91

[11] Shinagawa K, Omori T, Oikawa K et al (2009) Ductility enhancement by boron addition in Co–Al–W high-temperature alloys. Scr Mater 61:612–615

[12] Ooshima M, Tanaka K, Okamoto NL et al (2010) Effects of quaternary alloying elements on the γ' solvus temperature of Co–Al–W based alloys with fcc/$L1_2$ two-phase microstructures. J Alloys Compd 508:71–78

[13] Xu YT, Xia TD, Zhao WJ, Wang XJ (2012) Alloying element Nb effect on microstructure of Co–Al–W superalloy by vacuum arc melting. Appl Mech Mater 229:63–67

[14] Xue F, Zhou HJ, Ding XF et al (2013) Improved high temperature γ' stability of Co–Al–W-base alloys containing Ti and Ta. Mater Lett 112:215–218

[15] Zhang L, Qu X, Qin M et al (2012) Microstructure and mechanical properties of γ' strengthened Co–Ni–Al–W-base ODS alloys. Mater Chem Phys 136:371–378

[16] Povstugar I, Choi P-P, Neumeier S et al (2014) Elemental partitioning and mechanical properties of Ti- and Ta-containing Co–Al–W-base superalloys studied by atom probe tomography and nanoindentation. Acta Mater 78:78–85

[17] Jiang C (2008) First-principles study of $Co_3(Al, W)$ alloys using special quasi-random structures. Scr Mater 59:1075–1078

[18] Chen M, Wang C-Y (2009) First-principles investigation of the site preference and alloying effect of Mo, Ta and platinum group metals in (Al, W). Scr Mater 60:659–662

[19] Xu WW, Han JJ, Wang Y et al (2013) First-principles investigation of electronic, mechanical and thermodynamic properties of $L1_2$ ordered $Co_3(M, W)$ (M = Al, Ge, Ga) phases. Acta Mater 61:5437–5448

[20] Saal JE, Wolverton C (2013) Thermodynamic stability of Co–Al–W $L1_2$ γ'. Acta Mater 61:2330–2338

[21] Meher S, Banerjee R (2014) Partitioning and site occupancy of Ta and Mo in Co base γ/γ' alloys studied my atom probe. Intermetallics 49:138–142

[22] Knop M, Mulvey P, Dye D et al (2014) A new polycrystalline Co–Ni superalloy. JOM 66:2495–2501

[23] Meher S, Carroll LJ, Pollock TM, Carroll MC (2016) Solute partitioning in multi-component γ/γ' Co–Ni base superalloys with near-zero lattice misfit. Scr Mater 113:185–189

[24] Feng G, Li H, Li SS, Sha JB (2012) Effect of Mo additions on microstructure and tensile behavior of a Co–Al–W–Ta–B alloy at room temperature. Scr Mater 67:499–502

[25] Xue F, Li ZQ, Feng Q (2010) Mo effect on the microstructure in Co–Al–W-based superalloys. In: Nie JF, Morton A (eds) Materials Science Forum. Trans Tech Publ, pp 420–423
[26] Makineni SK, Nithin B, Chattopadhyay K (2015) A new tungsten free γ–γ′ Co–Al–Mo–Nb-based superalloy. Scr Mater 98:36–39
[27] Makineni SK, Nithin B, Chattopadhyay K (2015) Synthesis of a new tungsten free γ–γ′ Co-based superalloy by tuning alloying additions. Acta Mater 85:85–94
[28] Makineni SK, Samanta A, Rojhirunsakool T et al (2015) A new class of high strength high temperature Co-based γ–γ′ Co–Mo–Al alloys stabilized with Ta addition. Acta Mater 97:29–40
[29] Davis JR, Mills KM, Lampman SR (1990) In: Metals handbook, vol 1. Properties and selection: irons, steels, and high-performance alloys. ASM Int. Mater. Park, Ohio, p 1063
[30] ASTM E562-11 (2011) Test method for determining volume fraction by systematic manual point count. ASTM International
[31] Aaronson HI, Pande CS (1998) A synthesis of mechanisms for initiation of the cellular (or discontinuous precipitation) reaction. Acta Mater 47:175–181
[32] Findik F (1998) Discontinuous (cellular) precipitation. J Mater Sci Lett 17:79–83
[33] Anantharaman TR, Ramaswamy V, Butler EP (1974) Effect of matrix precipitation on cellular growth kinetics in an Al-28 at.% Zn alloy. J Mater Sci 9:240–244
[34] Vijayalakshmi M, Seetharaman V, Raghunathan VS (1982) Cellular decomposition in Al-Zn alloys. Acta Metall 30:1147–1156
[35] Manna I, Gust W, Predel B (1990) Discontinuous precipitation in Zn–Al alloys. Scr Metall Mater 24:1635–1640
[36] Vijayalakshmi M, Seetharaman V, Raghunathan VS (1982) Morphological features of discontinuous reactions in Al–Zn alloys. Mater Sci Eng 52:249–256
[37] Abdou S, Solórzano G, El-Boragy M et al (1996) In-situ study of discontinuous precipitation in Al-15 at.% Zn. Scr Mater 34:1431–1436
[38] Yang CF, Sarkar G, Fournelle RA (1988) Discontinuous precipitation and coarsening in Al–Zn alloys. Acta Metall 36:1511–1520
[39] Kobayashi S, Tsukamoto Y, Takasugi T et al (2009) Determination of phase equilibria in the Co-rich Co–Al–W ternary system with a diffusion-couple technique. Intermetallics 17:1085–1089
[40] Lass EA, Williams ME, Campbell CE et al (2014) γ′ Phase stability and phase equilibrium in ternary Co–Al–W at 900 °C. J Phase Equilibria Diffus 35:711–723
[41] Tu KN, Turnbull D (1967) Morphology of cellular precipitation of tin from lead–tin bicrystals. Acta Metall 15:369–376
[42] Fournelle RA, Clark JB (1972) The genesis of the cellular precipitation reaction. Metall Trans 3:2757–2767
[43] Pessah M, Caron P, Khan T (1992) Effect of mu phase on the mechanical properties of a nickel-base single crystal superalloy. In: Antonlovitch SD, Stusrud RW (eds) Superalloys 1992, TMS Warrendale, PA, pp 567–576
[44] Simonetti M, Caron P (1998) Role and behaviour of μ phase during deformation of a nickel-based single crystal superalloy. Mater Sci Eng, A 254:1–12
[45] Shi Q, Ding X, Chen J et al (2014) Fracture mode of a Ni-based single crystal superalloy containing topologically close-packed phases at ambient temperature. Metall Mater Trans A 45:1665–1669
[46] Hobbs RA, Zhang L, Rae CMF, Tin S (2008) TCP suppression in a ruthenium-bearing single-crystal nickel-based superalloy. JOM 60:37–42
[47] Yang JX, Zheng Q, Sun XF et al (2007) Topologically close-packed phase precipitation in a nickel-base superalloy during thermal exposure. Mater Sci Eng, A 465:100–108
[48] Mousavi Anijdan SH, Bahrami A (2005) A new method in prediction of TCP phases formation in superalloys. Mater Sci Eng, A 396:138–142
[49] Rae CMF, Karunaratne MSA, Small CJ et al (2000) Topologically close packed phases in an experimental rhenium-containing single crystal superalloy. Superalloys 2000:767–776
[50] Sinha AK (1972) Topologically close-packed structures of transition metal alloys. Prog Mater Sci 15:88–93
[51] Gan W, Zhanpeng J (1990) phase equilibria in Mo–Co–Ni and Mo–Ni–Fe systems at 1000 °C. J Less-Common Met 160:29–33
[52] Sinha AK (1972) Topologically close-packed structures of transition metal alloys. Prog Mater Sci 15:93–98
[53] Sinha AK (1972) Topologically close-packed structures of transition metal alloys. Prog Mater Sci 15:111–114
[54] Rae CMF, Reed RC (2001) The precipitation of topologically close-packed phases in rhenium-containing superalloys. Acta Mater 49:4113–4125
[55] Chen JY, Feng Q, Sun ZQ (2010) Topologically close-packed phase promotion in a Ru-containing single crystal superalloy. Scripta Mater 63:795–798
[56] Pessah-Simonetti M, Donnadieu P, Caron P (1994) T.C.P. phase particles embedded in a superalloy matrix: interpretation and prediction of the orientation relationships. Scripta Metall. Mater. 30:1553–1558
[57] Matuszewski K, Rettig R, Matysiak H, Peng Z, Povstugar I, Choi P et al (2015) Effect of ruthenium on the precipitation

of topologically close packed phases in Ni-based superalloys of 3rd and 4th generation. Acta Mater 95:274–283

[58] Matuszewski K, Rettig R, Rasiński M, Kurzydłowski KJ, Singer RF (2014) The three-dimensional morphology of topologically close packed phases in a high rhenium containing nickel-based superalloy. Adv Eng Mater 16:171–175

[59] Nabarro FRN (1996) Rafting in superalloys. Metall Mater Trans A 27:513–530

[60] Makineni SK, Nithin B, Chattopadhyay K (2016) Effect of Cr on Co(Ni)–Al–Mo–Nb based γ–γ′ alloys (under preparation)